

Toward Real-world Infrared Image Super-Resolution: A Unified Autoregressive Framework and Benchmark Dataset

Yang Zou^{1†}, Jun Ma^{2†}, Zhidong Jiao², Xingyuan Li³, Zhiying Jiang⁴, Jinyuan Liu^{2*}

¹ School of Computer Science, Northwestern Polytechnical University

² School of Software Technology & DUT-RU International School of ISE, Dalian University of Technology

³ School of Computer Science, Zhejiang University

⁴ College of Information Science and Technology, Dalian Maritime University

archerv2@mail.nwpu.edu.cn atlantis918@hotmail.com



Figure 1. Overview of the constructed **FLIR-IISR** dataset. To bridge the gap between synthetic and real-world infrared image super-resolution (IISR), we construct the **FLIR-IISR** dataset using a FLIR T1050sc camera at a 1024×768 resolution, which contains 1,457 paired LR–HR images captured across 6 cities, 3 seasons, and 2 real blur patterns of optical and motion blur across 12 scene categories.

Abstract

Infrared image super-resolution (IISR) under real-world conditions is a practically significant yet rarely addressed task. Pioneering works are often trained and evaluated on simulated datasets or neglect the intrinsic differences between infrared and visible imaging. In practice, however, real infrared images are affected by coupled optical and sensing degradations that jointly deteriorate both structural sharpness and thermal fidelity. To address these challenges, we propose **Real-IISR**, a unified autoregressive framework for real-world IISR that progressively reconstructs fine-grained thermal structures and clear backgrounds in a scale-by-scale manner via thermal-structural guided visual autoregression. Specifically, a Thermal-Structural Guidance module encodes thermal priors to miti-

gate the mismatch between thermal radiation and structural edges. Since non-uniform degradations typically induce quantization bias, **Real-IISR** adopts a Condition-Adaptive Codebook that dynamically modulates discrete representations based on degradation-aware thermal priors. Also, a Thermal Order Consistency Loss enforces a monotonic relation between temperature and pixel intensity, ensuring relative brightness order rather than absolute values to maintain physical consistency under spatial misalignment and thermal drift. We build **FLIR-IISR**, a real-world IISR dataset with paired LR–HR infrared images acquired via automated focus variation and motion-induced blur. Extensive experiments demonstrate the promising performance of **Real-IISR**, providing a unified foundation for real-world IISR and benchmarking. The dataset and code are available at: <https://github.com/JZD151/Real-IISR>.

[†] Equal contribution. ^{*} Corresponding author.

1. Introduction

Infrared image super-resolution (IISR) is essential for various perception tasks like object detection, target tracking, and autonomous driving under low-light or adverse conditions [12, 14, 15, 50, 57]. Recent advances in real-world image super-resolution [9, 31, 42, 46] have substantially improved the reconstruction quality of visible images. However, extending such progress to the infrared domain remains highly non-trivial. The longer wavelengths and weaker atmospheric scattering in infrared sensing lead to spatially varying blur, unstable thermal boundaries, and temperature-dependent radiometric drift, which together form complex, coupled degradations [19–21, 45]. These challenges make real-world IISR a unique and fundamentally difficult problem.

Previous studies on real-world image super-resolution (ISR) have largely addressed complex degradations. RealSR [1] pioneered paired data collection via focal-length variation, while BSRGAN [53] and Real-ESRGAN [41] introduced effective degradation pipelines for blind ISR. Building on these advances, diffusion-based [5, 16, 35, 40, 42, 46, 49] and visual autoregressive [11, 31] models further improved perceptual fidelity. However, the stochastic sampling of diffusion models and the absence of infrared degradation priors limit their applicability to real-world IISR [6, 24, 31, 40, 46].

On the other hand, recent IISR methods exploit sensing-specific properties to compensate for weak high-frequency details. ChasNet [28] enhances informative channels via channel-split convolutions, while CoRPLE [14] and CRG [57] introduce contourlet-domain residual modeling with prompt guidance. DifIISR [15] further integrates gradient-based alignment and perceptual priors within diffusion. Despite their progress, these approaches rely on simplified degradations, limiting their robustness to complex real-world infrared degradations.

While prior studies have advanced real-world and infrared super-resolution (SR), two fundamental challenges remain for real-world IISR. **(1) Lack of real infrared degradation datasets.** Existing IISR methods are typically trained on downsampled Infrared and Visible Image Fusion (IVIF) datasets, which fail to capture the coupled optical–sensor degradations of real infrared imaging, leading to poor generalization. **(2) Absence of infrared-aware degradation modeling.** Diffusion-based SR networks rely on fixed degradation priors, overlooking spatially heterogeneous blur and noise [13, 25, 31, 40, 46]. Meanwhile, visual autoregressive models [11, 31] are confined to visible images, lacking infrared-specific constraints where thermal intensity often misaligns with structural edges, causing boundary distortion and thermal drift.

To this end, we construct a real-world IISR dataset, **FLIR-IISR**, inspired by RealSR [1]. As shown in Fig. 1,

it contains 1,457 real captured LR–HR pairs acquired with a FLIR T1050sc camera at a 1024×768 resolution, spanning 12 scenes across 6 cities, and 3 seasons. LR images were obtained by automated focus variation and real object motion to produce realistic defocus and motion blur degradations, providing a new benchmark for real-world IISR.

We also propose **Real-IISR**, a unified autoregressive framework for real-world IISR. Specifically, Real-IISR proposes a Thermal-Structural Guidance (TSG) module that explicitly encodes thermal intensity and edge-aware structural cues to bridge the inherent mismatch between heat distributions and object boundaries, enabling structure-consistent and thermally stable reconstruction. To correct quantization bias and maintain thermal fidelity under spatially nonuniform blur and noise, Real-IISR introduces a Condition-Adaptive Codebook (CAC) that dynamically modulates discrete embeddings according to infrared degradation priors. Given the monotonic property of infrared imaging, where higher temperatures correspond to higher pixel intensities [8, 33], Real-IISR further adopts a Thermal Order Consistency Loss that enforces relative order consistency between patch pairs and remains robust to LR–HR misalignment in real-world infrared data. Our contributions are summarized as follows:

- We construct **FLIR-IISR**, a real-world IISR dataset comprising 1,457 LR–HR pairs with real-world degradations, thereby providing a new benchmark for real-world IISR.
- We propose **Real-IISR**, a unified autoregressive framework guided by thermal priors that adaptively handles heterogeneous infrared degradations.
- Extensive experiments on both the proposed FLIR-IISR dataset and simulated dataset demonstrate the impressive performance of our method.

2. Related work

2.1. Image Super-Resolution

Early methods [17, 44, 55] assume simple degradations, which limit their generalization to real-world conditions. RealSR [1] mitigates this gap by capturing paired LR–HR samples under varying focal lengths, while later works [47, 52] improve realism yet remain sensitive to spatially variant blur and compound noise. Generative frameworks, including GAN-based [41, 53], diffusion-based [37, 42], and autoregressive models [11, 31, 34], further enhance perceptual fidelity via learned priors.

Extending such approaches to infrared imaging remains challenging due to wavelength-dependent blur, nonlinear radiometric responses, and unstable thermal boundaries [7, 26, 30, 56, 58]. IISR methods, such as ChasNet [28], CoRPLE [14], CRG [57], and DifIISR [15], largely address these issues but often rely on synthetic degradations, hindering their robustness in real-world conditions.

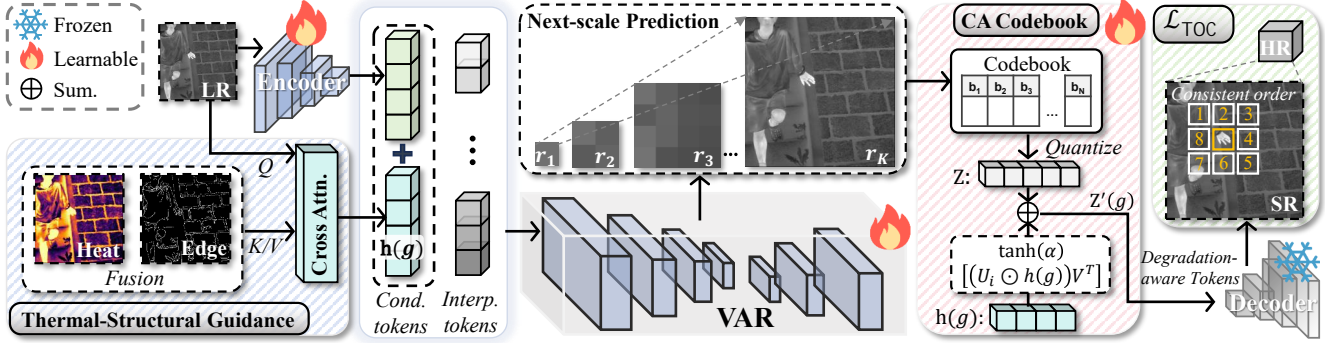


Figure 2. Overview of Real-IISR. The Thermal-Structural Guidance (TSG) module fuses thermal priors for degradation-aware encoding. The VAR backbone performs scale-by-scale generation via next-scale prediction, while the Condition-Adaptive Codebook (CAC) dynamically adjusts quantized embeddings based on degradation-aware priors for thermal fidelity. Finally, the Thermal Order Consistency Loss \mathcal{L}_{TOC} preserves physically consistent thermal ordering.

2.2. Visual Autoregressive Models

Visual Autoregressive (VAR) models model conditional dependencies for token-wise generation with global structural control. Early patch-based methods [27, 39] suffered from limited receptive fields and poor semantic consistency. Subsequent hierarchical designs such as VQ-VAE-2 [32] and VQGAN [4] introduced multi-scale codebooks and adversarial quantization, improving perceptual fidelity and enabling scale-by-scale generation. The VAR framework [38] further formalized “next-scale prediction,” achieving efficient coarse-to-fine synthesis. Applied to SR, VARSR [31] integrates positive-negative pairs for stable reconstruction, yet its unified sampling remains susceptible to local blur and texture breaks under complex degradations.

3. Method

Overview. Real-world IISR is inherently challenging due to complex optical-sensor degradations and the weak correlation between thermal intensity and structural edges. To address these issues, we propose a unified autoregressive framework for high-fidelity and physically consistent IISR, as illustrated in Fig. 2. The framework comprises three key components: (1) Thermal-Structural Guidance (TSG), which explicitly encodes heat source semantics and structural edges to align thermal distributions with spatial boundaries; (2) Condition-Adaptive Codebook (CAC), which dynamically modulates codebook embeddings with degradation-aware priors to enhance texture realism and robustness under diverse degradations; and (3) Thermal Order Consistency Loss \mathcal{L}_{TOC} , which preserves the monotonic thermal-intensity relationship between SR and HR, mitigating thermal drift and boundary distortion. Together, these components enable our model to produce geometrically consistent, texture-rich, and thermally reliable infrared reconstructions under real-world degradations.

3.1. Thermal-Structural Guidance

Infrared imaging inherently suffers from the weak correspondence between thermal intensity and structural boundaries. For instance, although a car engine acts as a strong heat source, its thermal radiation region often deviates from the actual contour of the vehicle. Training a generative model directly on such images can cause it to overfit thermal peaks while neglecting real edges, leading to structural distortion and thermal drift in the reconstructed results. To mitigate this issue, we introduce a Thermal-Structural Guidance (TSG) module that explicitly encodes thermal semantics and structural cues as dual guidance.

Based on the low-resolution input (\mathbf{I}_{LR}), we construct two auxiliary representations: a heat map (\mathbf{I}_{Heat}) to provide semantic heat-source information, and an edge map (\mathbf{I}_{Edge}) to capture geometric boundaries, as shown in Fig. 2. Each map is processed through a dedicated encoder $\mathbf{F}_{\text{Heat}} = \text{Enc}_T(\mathbf{I}_{\text{Heat}})$ and $\mathbf{F}_{\text{Edge}} = \text{Enc}_S(\mathbf{I}_{\text{Edge}})$, where Enc_T and Enc_S are pre-trained encoders based on the DINOv3 [36]. To combine the two modalities, we use an adaptive weighting mechanism that fuses local and global cues. A learnable attention gate $\mathbf{W} = \sigma(L(\mathbf{A}) + G(\mathbf{A}))$, where $\mathbf{A} = \mathbf{F}_{\text{Heat}} + \mathbf{F}_{\text{Edge}}$, adaptively balances the contributions of thermal and structural features. Here, $L(\cdot)$ and $G(\cdot)$ represent local and global attention operators, and $\sigma(\cdot)$ denotes the sigmoid function. The fused guidance is computed as:

$$\mathbf{F}_{\text{Fused}} = \mathbf{F}_{\text{Heat}} \odot \mathbf{W} + \mathbf{F}_{\text{Edge}} \odot (\mathbf{1} - \mathbf{W}), \quad (1)$$

where \odot denotes element-wise multiplication. This design enables spatially adaptive fusion, which regions with salient thermal patterns rely more on \mathbf{F}_{Heat} , and those with clear structural boundaries emphasize \mathbf{F}_{Edge} .

The fused representation $\mathbf{F}_{\text{Fused}}$ serves as a semantic-structural layout prior to guide the low-resolution feature $\mathbf{F}_{\text{LR}} = \text{Enc}_T(\mathbf{I}_{\text{LR}})$. We employ a cross-attention

module to propagate aligned information as $\mathbf{F}_{\text{TSG}} = \text{Softmax}\left(\frac{QK^\top}{\sqrt{d}}\right)V$, where $Q = \mathbf{W}_Q\mathbf{F}_{\text{LR}}$, $K = \mathbf{W}_K\mathbf{F}_{\text{Fused}}$, and $V = \mathbf{W}_V\mathbf{F}_{\text{Fused}}$. \mathbf{W}_Q , \mathbf{W}_K , and \mathbf{W}_V are learnable linear projections, and d denotes the feature dimension for scaling. This prevents the model from overfitting to high-intensity thermal regions and encourages accurate boundary reconstruction. Empirically, this results in improved contour sharpness, reduced thermal drift, and enhanced physical interpretability in super-resolved infrared images.

3.2. Condition-Adaptive Codebook

Real infrared images often suffer from complex, spatially non-uniform degradations such as defocus blur, motion blur, and sensor noise [14, 15]. These degradations not only distort local textures but also introduce code selection bias in autoregressive models, where incorrect discrete tokens may be activated under unstable degradation patterns. Moreover, the inherent quantization in VQ-VAE [39] introduces discretization errors that prevent the precise recovery of details, even with accurate code selection [11, 31]. Consequently, the reconstructed images may exhibit over-smoothed textures and weakened structural fidelity.

To overcome these issues, we propose a Condition-Adaptive Codebook (CAC), which dynamically refines codebook embeddings based on degradation-aware priors. As shown in Fig. 2, instead of performing a static table lookup, each code embedding is adaptively modulated through low-rank perturbations conditioned on the low-resolution observation and cues such as thermal distributions and edge structures. Therefore, the same discrete index can decode to different embedding vectors under different degradation conditions and scenes. This design enables the model to adaptively refine decoded features while maintaining stable discrete semantics, thus reducing quantization bias and improving texture realism. Formally, the code embedding update process is defined as:

$$\mathbf{Z}'(g)[i] = \mathbf{Z}[i] + \tanh(\alpha) [(\mathbf{U}_i \odot \mathbf{h}(g))\mathbf{V}^\top], \quad (2)$$

where $\mathbf{Z}[i] \in \mathbb{R}^d$ denotes the basic embedding of the i -th code, $\mathbf{U}_i \in \mathbb{R}^r$ is the low-rank basis vector for that code, $\mathbf{V} \in \mathbb{R}^{d \times r}$ represents the shared feature direction matrix, and $\mathbf{h}(g) \in \mathbb{R}^r$ is a condition vector derived from \mathbf{F}_{TSG} , incorporating cues such as thermal distributions and edge structures. \odot denotes element-wise multiplication, and $\tanh(\alpha)$ is a gating factor that constrains the perturbation magnitude to ensure stable optimization.

By enabling code embeddings to vary adaptively with degradation conditions, the proposed CAC effectively mitigates code selection bias and quantization artifacts, yielding more structurally consistent and texture-rich infrared reconstructions under real-world degradations.

3.3. Optimization

Following the VAR [38], we employ a cross-entropy loss \mathcal{L}_{CE} to supervise the Transformer-based autoregressive module at the token level. However, even with correct code selection, quantization in VQ-VAE [39] inevitably introduces discretization errors, leading to texture degradation and loss of fine details. To alleviate this issue, our Condition-Adaptive Codebook adaptively refines code embeddings, while an additional pixel-level reconstruction loss is introduced to provide continuous supervision. Specifically, an MSE loss \mathcal{L}_{MSE} is applied between the SR and HR images to improve fidelity. Yet, real infrared degradations, such as defocus and motion blur, cause spatially varying peak shifts and local temperature compression, where simple pixel-wise MSE fails to restore physically accurate thermal distributions.

To address this, we propose a Thermal Order Consistency Loss \mathcal{L}_{TOC} that enforces the monotonic relationship between temperature and pixel intensity. Unlike MSE, which relies on absolute values, \mathcal{L}_{TOC} constrains relative thermal ordering between SR and HR pairs, penalizing cases where brightness order is reversed due to LR-HR misalignment and heat diffusion. This preserves local temperature gradients and stabilizes heat-source contrast. Formally, it is defined as:

$$\mathcal{L}_{\text{TOC}} = \frac{1}{|\Omega|} \sum_{(i,j) \in \Omega} \text{ReLU}\left(-[(\mathbf{I}_{\text{SR}}^p(i) - \mathbf{I}_{\text{SR}}^p(j)) \times (\mathbf{I}_{\text{HR}}^p(i) - \mathbf{I}_{\text{HR}}^p(j))]\right), \quad (3)$$

where Ω denotes the set of adjacent patches, and \mathbf{I}_{SR}^p and \mathbf{I}_{HR}^p are the SR and HR patches, respectively. The ReLU term penalizes inverted thermal ordering between patch pairs, thereby enforcing physically consistent monotonicity of infrared intensity. This patch-wise formulation ensures robustness to minor spatial misalignments while maintaining correct local temperature ordering, effectively mitigating thermal peak drift in the reconstructed results. Finally, the overall training objective is defined as:

$$\mathcal{L}_{\text{total}} = \mathcal{L}_{\text{CE}} + \lambda_1 \mathcal{L}_{\text{MSE}} + \lambda_2 \mathcal{L}_{\text{TOC}}, \quad (4)$$

where \mathcal{L}_{CE} supervises token prediction, \mathcal{L}_{MSE} ensures pixel-level fidelity, and \mathcal{L}_{TOC} enforces physical consistency of thermal distributions. The coefficients λ_1 and λ_2 balance the contribution of each term.

3.4. FLIR-IISR

As shown in Fig. 1, we construct FLIR-IISR, a real-world IISR dataset that contains **1,457** paired LR–HR images captured across **6** cities, **3** seasons, and **2** real blur patterns of optical and motion blur across **12** scene categories, stored in lossless BMP format to preserve radiometric fidelity. LR



Figure 3. Data collection pipeline of FLIR-IISR.

and HR pairs may exhibit slight sub-pixel misalignment due to the defocus–refocus acquisition process.

As shown in Fig. 3, an automated capture program was developed to generate paired LR–HR data. Upon each electronic shutter trigger, the camera first performs automatic focusing to acquire a sharp HR image. Then, the program randomly adjusts the electronic focus ring to produce multiple defocus levels. One blurred frame is randomly selected and downsampled by 4× to obtain the LR counterpart. This process ensures consistent viewpoints while providing realistic degradations, including defocus and motion blur caused by moving objects.

FLIR-IISR provides dual-level annotations: degradation labels and scene labels. In the degradation dimension, the dataset contains 1,305 images with defocus blur and 152 with motion blur. In the semantic dimension, it covers 12 scene categories: person (309), bicycle (22), motorcycle (27), tricycle (13), car (234), bus (5), plane (54), statue (157), regular object (248), building (706), road (132), and complex scene (401), as shown in Fig. 1. Note that an image may contain multiple scene categories. This hierarchical annotation makes FLIR-IISR a comprehensive and practical benchmark for evaluating real-world IISR performance.

4. Experiments

4.1. Experimental Settings

Implementation Details. Our Real-IISR was trained on 4 NVIDIA A800 GPUs. To accelerate the training, we utilized the pre-trained VAR and VQVAE from [31]. The training process employs the AdamW [23] optimizer with a batch size of 4, a weight decay of 5×10^{-2} , and a learning rate of 5×10^{-5} . The model is fine-tuned for 10k iterations. For loss balancing, we set $\lambda_1 = 0.2$ and $\lambda_2 = 0.8$. In computing the Thermal Order Consistency Loss \mathcal{L}_{TOC} , the patch size is empirically set to 8. For the Condition-Adaptive Codebook, the rank of the low-rank modulation is set to $r = 8$ in all experiments.

Datasets and Metrics. We train our model on the FLIR-IISR dataset with 1,192 images for training and 265 for testing, and evaluate it together with 500 test images selected from the M³FD [18] dataset. Following the experimental settings in [31, 40], the resolution of HR images is set to 512×512, while that of LR images is set to 128×128 during both training and testing. To mitigate overfitting, random cropping is employed as a data augmentation strategy.

For a comprehensive quantitative evaluation, we adopt three reference-based and two no-reference image quality metrics. To assess the reconstruction fidelity with respect to HR images, we compute PSNR, SSIM [43], and LPIPS [54]. In addition, to evaluate the perceptual quality of the generated images without reference, we employ MUSIQ [10] and MANIQA [48].

Comparitive Methods. We conduct a comprehensive comparison with nine state-of-the-art methods, including three image super-resolution (ISR) methods: HAT [2], BI-DiffSR [3], and PFT-SR [22]; three infrared image super-resolution (IISR) methods: CoRPLE [14], InfraFFN [29], and DifIISR [15]; and three real-world image super-resolution (R-ISR) methods: RealSR [9], SinSR [42], and VARSR [31]. All comparative methods are retrained on the FLIR-IISR dataset with the same setting as Real-IISR.

4.2. Quantitative Comparison

No-reference Metrics Comparison. As shown in Tab. 1, our method is compared with nine competitive approaches on the FLIR-IISR and M³FD datasets. It achieves the highest scores on both metrics for the Set5 and Set15 subsets of FLIR-IISR, attains the best MUSIQ performance on M³FD, and maintains competitive results on MANIQA. The improvement in MUSIQ demonstrates that Real-IISR possesses a stronger capability in modeling global perceptual quality and structural consistency. By integrating thermal order consistency with structural priors during autoregressive reconstruction, Real-IISR effectively mitigates the coupled optical and perceptual degradations inherent in infrared imaging. Meanwhile, the stable MANIQA performance indicates that the model successfully preserves high-quality textures and edge details.

Reference-based Metrics Comparison. Tab. 2 presents quantitative comparisons on the FLIR-IISR and M³FD datasets using reference-based metrics. Real-IISR achieves the best overall performance across all subsets, demonstrating strong pixel-wise fidelity and perceptual consistency. This advantage verifies the effectiveness of the proposed Thermal Order Consistency Loss \mathcal{L}_{TOC} that enforces the monotonic relationship between temperature and pixel intensity, and the Condition-Adaptive Codebook, which enhances texture realism under spatially variant degradations. Benefiting from the joint modeling of thermal radiation and structural information, Real-IISR consistently reconstructs geometrically clear images under complex real-world degradations, achieving a well-balanced trade-off between structural fidelity and perceptual consistency.

4.3. Qualitative Results

Fig. 5 shows the qualitative comparisons on FLIR-IISR and M³FD datasets. For intuitive visualization, pseudo-color thermal maps are displayed to highlight the radiometric

Datasets			FLIR-IISR@Set5		FLIR-IISR@Set15		M ³ FD@Set5		M ³ FD@Set15	
Methods			MUSIQ↑	MANIQA↑	MUSIQ↑	MANIQA↑	MUSIQ↑	MANIQA↑	MUSIQ↑	MANIQA↑
Low Resolution	-	-	27.9188	0.2030	25.4302	0.1740	24.2688	0.1438	24.7427	0.1770
High Resolution	-	-	55.1375	0.3333	51.8250	0.3036	22.6813	0.1626	28.7760	0.2149
HAT [2]	CVPR'23	ISR	40.9844	0.2843	33.9990	0.2349	22.2281	0.1822	25.5260	0.2351
BI-DiffSR [3]	NIPS'24	ISR	37.6250	0.2279	32.5854	0.1883	19.8031	0.1354	25.7417	0.1755
PFT-SR [22]	CVPR'25	ISR	41.1875	0.2847	33.9823	0.2366	22.3563	0.1769	25.7583	0.2393
CoRPLe [14]	ECCV'24	IISR	32.3094	0.2256	27.8458	0.2101	23.6844	0.1802	25.9229	0.2426
InfraFFN [29]	KBS'25	IISR	36.8250	0.2393	30.9240	0.2226	22.1625	0.1766	25.0010	0.2346
DifIISR [15]	CVPR'25	IISR	<u>54.7875</u>	0.3672	<u>53.1625</u>	0.3310	40.4563	0.2801	48.1625	<u>0.3248</u>
RealSR [9]	CVPR'20	R-ISR	41.1844	0.2883	39.5490	0.2543	21.1906	0.1572	27.6917	0.2261
SinSR [42]	CVPR'24	R-ISR	54.1625	<u>0.3719</u>	53.0854	<u>0.3342</u>	<u>40.9125</u>	0.2277	<u>48.3479</u>	0.3348
VARSR [31]	ICML'25	R-ISR	52.7625	0.2948	51.9969	0.2995	38.9438	<u>0.2776</u>	39.9427	0.3003
Ours	-	R-IISR	59.9000	0.3776	57.0625	0.3403	41.5750	0.2532	49.0458	0.3074

Table 1. No-reference Metrics Comparison on FLIR-IISR and M³FD datasets. The best is in **bold**, while the second is underlined. For M³FD, Set5/15 are randomly sampled subsets. For FLIR-IISR, Set5/15 corresponds to motion/optical blur.

Datasets			FLIR-IISR@Set5			FLIR-IISR@Set15			M ³ FD@Set5			M ³ FD@Set15		
Methods			PSNR↑	SSIM↑	LPIPS↓	PSNR↑	SSIM↑	LPIPS↓	PSNR↑	SSIM↑	LPIPS↓	PSNR↑	SSIM↑	LPIPS↓
BI-DiffSR [3]	NIPS'24	ISR	<u>27.1976</u>	0.7869	0.4218	<u>28.7676</u>	0.8049	0.5206	35.9204	0.9062	0.3235	34.8666	0.8644	0.3133
DifIISR [15]	CVPR'25	IISR	27.1969	<u>0.8195</u>	0.2525	28.5603	0.8474	0.2739	<u>35.8423</u>	0.9318	0.2474	<u>34.6620</u>	0.9114	0.2214
SinSR [42]	CVPR'24	R-ISR	26.7594	0.6970	0.3670	28.3163	0.8521	0.2956	35.1806	<u>0.9323</u>	0.2528	34.0048	0.9041	<u>0.1652</u>
VARSR [31]	ICML'25	R-ISR	26.9767	0.7868	<u>0.2304</u>	28.3439	<u>0.8613</u>	<u>0.2003</u>	33.6762	0.9268	<u>0.2436</u>	32.6001	0.8997	0.1895
Ours	-	R-IISR	28.5126	0.8278	0.1615	29.5136	0.8895	0.1340	32.3175	0.9383	0.1997	31.5633	<u>0.9047</u>	0.1361

Table 2. Reference-based Metrics Comparison on FLIR-IISR and M³FD datasets. The best is in **bold**, while the second is underlined. For M³FD, Set5/15 are randomly sampled subsets. For FLIR-IISR, Set5/15 corresponds to motion/optical blur.

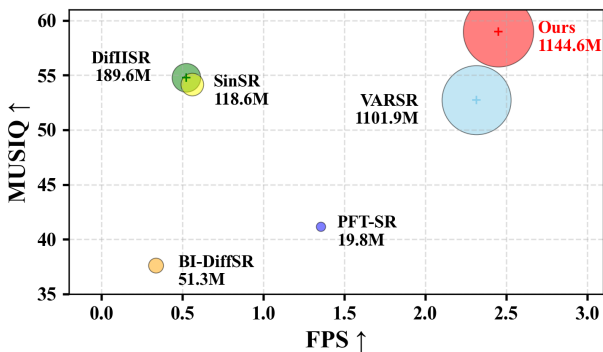


Figure 4. Efficiency comparison in terms of perceptual MUSIQ and FPS; circle diameter indicates model parameters.

consistency of different methods, and the graph illustrates grayscale fluctuations along the sampling line. Competing methods often produce blurred contours, unstable thermal regions, or over-enhanced hotspots due to insufficient ther-

mal perception. In contrast, Real-IISR reconstructs sharper edges and faithful heat distributions with fewer artifacts, and the Thermal Order Consistency Loss \mathcal{L}_{TOC} further ensures the monotonic relationship between temperature and pixel intensity to avoid thermal peak drift. For instance, in the water pipe region of the third row, IISR methods (e.g., DifIISR and CoRPLe) tend to generate unstable thermal boundaries, while R-ISR methods (e.g., VARSR and RealSR) fail to preserve the correct temperature and generate notable artifacts. The Thermal-Structural Guidance aligns heat radiation with object boundaries, while the Condition-Adaptive Codebook enhances fine-grained texture details under spatially varying degradations. Real-IISR preserves both edge sharpness and thermal uniformity, demonstrating its advantage in maintaining structural fidelity and physically consistent thermal patterns.

4.4. Efficiency Analysis

We evaluate model efficiency in terms of parameters and inference speed (FPS) on a single NVIDIA A800 GPU.

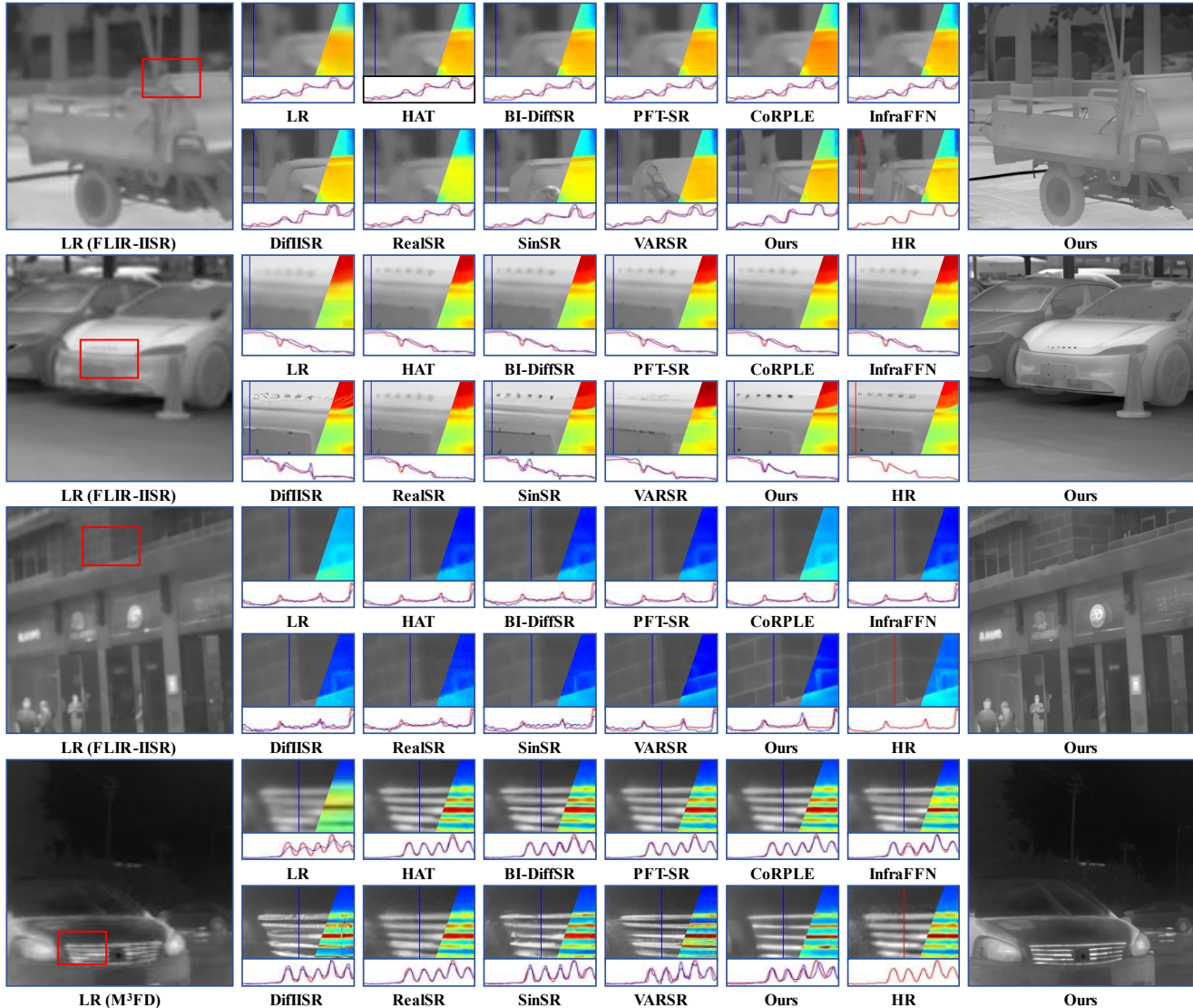


Figure 5. Qualitative comparison of IISR with SOTA methods on FLIR-IISR and M^3FD datasets. The graph illustrates grayscale fluctuations along the blue-marked sampling line, and red-marked sampling line denotes the HR.

As shown in Fig. 4, Real-IISR, though the largest model (1144.6 M), achieves the fastest inference (2.45 FPS) and best perceptual quality. Diffusion-based methods are slowed by multi-step denoising, while autoregressive frameworks enable deterministic generation with higher throughput. Compared to the VAR-based VARSR [31] that adopts a diffusion-based refiner to gradually refine the generated results, Real-IISR achieves **6% faster** inference despite being slightly larger in size, owing to its concise architecture, demonstrating superior computational efficiency.

4.5. Ablation Study

Effectiveness of TSG and CAC. To validate the contribution of the proposed Thermal-Structural Guidance (TSG)

and Condition-Adaptive Codebook (CAC), we perform an ablation study on the FLIR-IISR and M^3FD datasets, as summarized in Fig. 7 and visualized in Fig. 6. Removing TSG leads to inaccurate alignment between thermal radiation and object boundaries, causing blurred edges and weakened structural contours. Excluding CAC results in unstable textures and inconsistent heat distributions, reflected by a notable degradation in MUSIQ and SSIM. In contrast, combining both modules achieves the best overall performance. As shown in Fig. 6, our full model reconstructs sharper boundaries and faithful temperature, highlighting its effectiveness in maintaining structural fidelity and radiometric consistency.

Impact of Loss. To assess the effectiveness of the Thermal

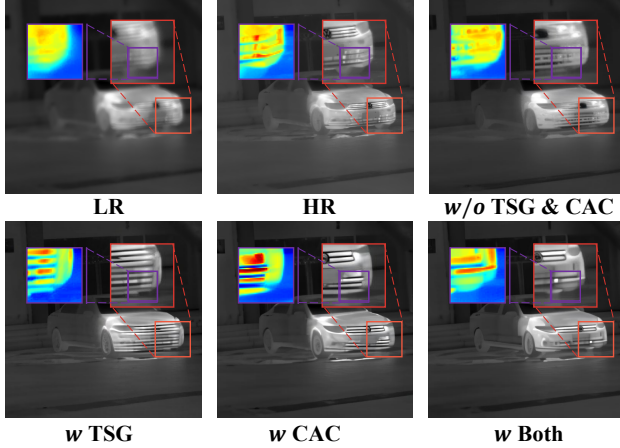


Figure 6. Qualitative ablation on the Thermal-Structural Guidance (TSG) and Condition-Adaptive Codebook (CAC).

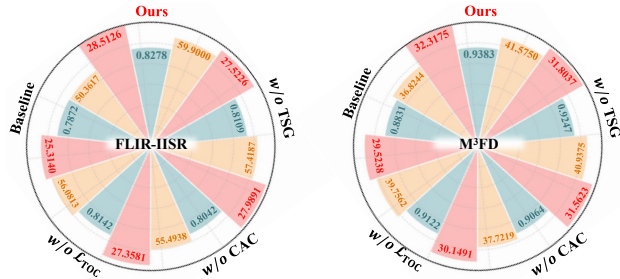


Figure 7. Quantitative ablation of TSG, CAC, and \mathcal{L}_{TOC} on PSNR, SSIM, and MUSIQ.

Order Consistency Loss \mathcal{L}_{TOC} , we conduct comparative experiments with and without this constraint. As shown in Fig. 8, removing the \mathcal{L}_{TOC} leads to disrupted thermal intensity ordering, resulting in thermal peak drift and local temperature compression. Correspondingly, Fig. 7 shows a notable drop in MUSIQ scores. Incorporating \mathcal{L}_{TOC} preserves the monotonic brightness–temperature relationship, yielding smoother and more coherent thermal distributions with improved physical consistency. This constraint effectively mitigates thermal peak shifts caused by non-uniform degradations, ensuring the radiometric reliability and visual stability of the reconstructed infrared images.

Choice of Generation Baseline. To examine the influence of the underlying generative paradigm, we replace the VAR backbone with a diffusion-based architecture (ResShift [51]) while keeping the same Thermal-Structural Guidance (TSG) as conditional input. As shown in Fig. 9, the diffusion-based variant fails to produce accurate results for both no-reference and reference-based evaluation, whereas the VAR-based framework achieves higher PSNR (28.51), lower LPIPS (0.1615), and better MUSIQ (59.90). This performance gap arises because iterative denoising in

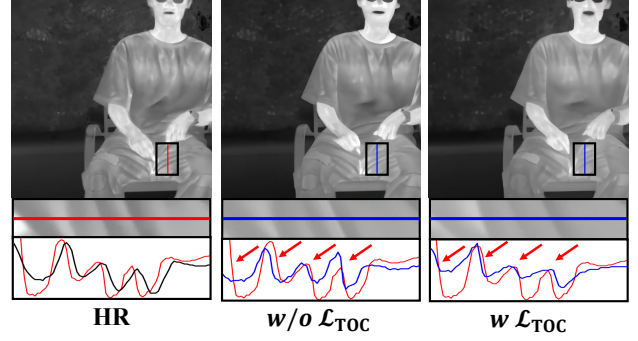


Figure 8. Qualitative ablation on the Thermal Order Consistency Loss \mathcal{L}_{TOC} with graph illustrates grayscale fluctuations along HR, LR, and models.

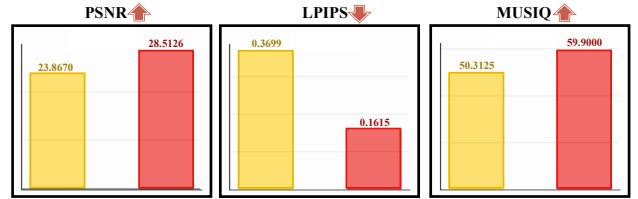


Figure 9. Quantitative ablation on the baseline choice of diffusion and VAR.

diffusion models tends to blur high-frequency thermal details and misalign structural cues, while the deterministic, token-level prediction in VAR preserves fine textures and consistent thermal–structural correspondence. These results verify that autoregressive generation better matches the discrete and spatially structured nature of real-world infrared imaging.

5. Conclusion

We tackle the challenge of real-world IISR, where synthetic degradations limit generalization to real scenarios. To bridge this gap, we introduce **FLIR-IISR**, a real-world paired dataset covering diverse scenes and physical degradations. Building on it, we propose **Real-IISR**, a unified autoregressive framework that aligns thermal and structural cues, adapts a Condition-Adaptive Codebook, and enforces the thermal ordering. Extensive experiments on both real and synthesised datasets show the impressive performance of our Real-IISR.

Broader Impact. The proposed FLIR-IISR dataset offers a new real-world benchmark for investigating infrared imaging degradations, thereby promoting progress toward realistic infrared restoration. Building on it, Real-IISR enhances thermal perception and structural fidelity, benefiting applications in autonomous driving, surveillance, and thermal monitoring under adverse conditions, establishing a solid foundation for realistic infrared restoration.

Acknowledgments

This work was partially supported by the China Post-doctoral Science Foundation (2023M730741) and the National Natural Science Foundation of China (No.62302078, No.62372080).

References

- [1] Jianrui Cai, Hui Zeng, Hongwei Yong, Zisheng Cao, and Lei Zhang. Toward real-world single image super-resolution: A new benchmark and a new model. In *Proceedings of the IEEE/CVF International Conference on Computer Vision*, pages 3086–3095, 2019. 2
- [2] Xiangyu Chen, Xintao Wang, Jiantao Zhou, Yu Qiao, and Chao Dong. Activating more pixels in image super-resolution transformer. In *Proceedings of the IEEE/CVF Conference on Computer Vision and Pattern Recognition*, pages 22367–22377, 2023. 5, 6
- [3] Zheng Chen, Haotong Qin, Yong Guo, Xiongfei Su, Xin Yuan, Linghe Kong, and Yulun Zhang. Binarized diffusion model for image super-resolution. *Proceedings of the Advances in Neural Information Processing Systems*, 37: 30651–30669, 2024. 5, 6
- [4] Patrick Esser, Robin Rombach, and Bjorn Ommer. Taming transformers for high-resolution image synthesis. In *Proceedings of the IEEE/CVF Conference on Computer Vision and Pattern Recognition*, pages 12873–12883, 2021. 3
- [5] Chengyu Fang, Chunming He, Fengyang Xiao, Yulun Zhang, Longxiang Tang, Yuelin Zhang, Kai Li, and Xiu Li. Real-world image dehazing with coherence-based pseudo labeling and cooperative unfolding network. *Proceedings of the Advances in Neural Information Processing Systems*, 37: 97859–97883, 2024. 2
- [6] Chengyu Fang, Chunming He, Longxiang Tang, Yuelin Zhang, Chenyang Zhu, Yuqi Shen, Chubin Chen, Guoxia Xu, and Xiu Li. Integrating extra modality helps segmentor find camouflaged objects well. *arXiv preprint arXiv:2502.14471*, 2025. 2
- [7] Yongsong Huang, Tomo Miyazaki, and et al. Liu, Xiaofeng. Infrared image super-resolution: A systematic review and future trends. *IEEE Journal of Selected Topics in Applied Earth Observations and Remote Sensing*, 2025. 2
- [8] Richard D Hudson. *Infrared system engineering*. Wiley-Interscience New York, 1969. 2
- [9] Xiaozhong Ji, Yun Cao, Ying Tai, Chengjie Wang, Jilin Li, and Feiyue Huang. Real-world super-resolution via kernel estimation and noise injection. In *Proceedings of the IEEE/CVF Conference on Computer Vision and Pattern Recognition Workshops*, pages 466–467, 2020. 2, 5, 6
- [10] Junjie Ke, Qifei Wang, Yilin Wang, Peyman Milanfar, and Feng Yang. Musiq: Multi-scale image quality transformer. In *Proceedings of the IEEE/CVF International Conference on Computer Vision*, pages 5148–5157, 2021. 5
- [11] Xiangtao Kong, Rongyuan Wu, Shuaizheng Liu, Lingchen Sun, and Lei Zhang. Nsarm: Next-scale autoregressive modeling for robust real-world image super-resolution. *arXiv preprint arXiv:2510.00820*, 2025. 2, 4
- [12] Huafeng Li, Zengyi Yang, Yafei Zhang, Wei Jia, Zhengtao Yu, and Yu Liu. Mulfs-cap: Multimodal fusion-supervised cross-modality alignment perception for unregistered infrared-visible image fusion. *IEEE Transactions on Pattern Analysis and Machine Intelligence*, 47(5):3673–3690, 2025. 2
- [13] Xingyuan Li, Yang Zou, Jinyuan Liu, Zhiying Jiang, Long Ma, Xin Fan, and Risheng Liu. From text to pixels: A context-aware semantic synergy solution for infrared and visible image fusion. *arXiv preprint arXiv:2401.00421*, 2023. 2
- [14] Xingyuan Li, Jinyuan Liu, Zhixin Chen, Yang Zou, Long Ma, Xin Fan, and Risheng Liu. Contourlet residual for prompt learning enhanced infrared image super-resolution. In *Proceedings of the European Conference on Computer Vision*, pages 270–288. Springer, 2024. 2, 4, 5, 6
- [15] Xingyuan Li, Zirui Wang, Yang Zou, Zhixin Chen, Jun Ma, Zhiying Jiang, Long Ma, and Jinyuan Liu. Diffisr: A diffusion model with gradient guidance for infrared image super-resolution. In *Proceedings of the IEEE/CVF Conference on Computer Vision and Pattern Recognition*, pages 7534–7544, 2025. 2, 4, 5, 6
- [16] Xinqi Lin, Jingwen He, Ziyang Chen, Zhaoyang Lyu, Bo Dai, Fanghua Yu, Yu Qiao, Wanli Ouyang, and Chao Dong. Diffbir: Toward blind image restoration with generative diffusion prior. In *Proceedings of the European Conference on Computer Vision*, pages 430–448. Springer, 2024. 2
- [17] Hongying Liu, Zubo Ruan, Peng Zhao, Chao Dong, Fanhua Shang, Yuanyuan Liu, Linlin Yang, and Radu Timofte. Video super-resolution based on deep learning: a comprehensive survey. *Artificial Intelligence Review*, 55(8):5981–6035, 2022. 2
- [18] Jinyuan Liu, Xin Fan, Zhanbo Huang, Guanyao Wu, Risheng Liu, Wei Zhong, and Zhongxuan Luo. Target-aware dual adversarial learning and a multi-scenario multi-modality benchmark to fuse infrared and visible for object detection. In *Proceedings of the IEEE/CVF Conference on Computer Vision and Pattern Recognition*, pages 5802–5811, 2022. 5
- [19] Jinyuan Liu, Xingyuan Li, Zirui Wang, Zhiying Jiang, Wei Zhong, Wei Fan, and Bin Xu. Promptfusion: Harmonized semantic prompt learning for infrared and visible image fusion. *IEEE/CAA Journal of Automatica Sinica*, 12(3):502–515, 2024. 2
- [20] Jinyuan Liu, Bowei Zhang, Qingyun Mei, Xingyuan Li, Yang Zou, Zhiying Jiang, Long Ma, Risheng Liu, and Xin Fan. Dcevo: Discriminative cross-dimensional evolutionary learning for infrared and visible image fusion. In *Proceedings of the Computer Vision and Pattern Recognition Conference*, pages 2226–2235, 2025.
- [21] Yating Liu, Yang Zou, Xingyuan Li, Xingyue Zhu, Kaiqi Han, Zhiying Jiang, Long Ma, and Jinyuan Liu. Toward a training-free plug-and-play refinement framework for infrared and visible image registration and fusion. In *Proceedings of the 33rd ACM International Conference on Multimedia*, pages 1268–1277, 2025. 2
- [22] Wei Long, Xingyu Zhou, Leheng Zhang, and Shuhang Gu. Progressive focused transformer for single image super-resolution. In *Proceedings of the IEEE/CVF Conference*

- on *Computer Vision and Pattern Recognition*, pages 2279–2288, 2025. 5, 6
- [23] Ilya Loshchilov, Frank Hutter, et al. Fixing weight decay regularization in adam. *arXiv preprint arXiv:1711.05101*, 5(5):5, 2017. 5
- [24] Yue Ma, Yingqing He, Xiaodong Cun, Xintao Wang, Siran Chen, Xiu Li, and Qifeng Chen. Follow your pose: Pose-guided text-to-video generation using pose-free videos. In *Proceedings of the AAAI Conference on Artificial Intelligence*, pages 4117–4125, 2024. 2
- [25] Yue Ma, Kunyu Feng, Xinhua Zhang, Hongyu Liu, David Junhao Zhang, Jinbo Xing, Yinhan Zhang, Ayden Yang, Zeyu Wang, and Qifeng Chen. Follow-your-creation: Empowering 4d creation through video inpainting. *arXiv preprint arXiv:2506.04590*, 2025. 2
- [26] Ziang Meng, Kaiqi Han, Yuchun He, Yuhan He, Xingyuan Li, and Yang Zou. Modeling detail feature connections for infrared image enhancement. *Neurocomputing*, 639:130200, 2025. 2
- [27] Achraf Oussidi and Azeddine Elhassouny. Deep generative models: Survey. In *2018 International Conference on Intelligent Systems and Computer Vision*, pages 1–8. IEEE, 2018. 3
- [28] Kalpesh Prajapati, Vishal Chudasama, Heena Patel, Anjali Sarvaiya, Kishor P Upla, Kiran Raja, Raghavendra Ramachandra, and Christoph Busch. Channel split convolutional neural network (chasnet) for thermal image super-resolution. In *Proceedings of the IEEE/CVF Conference on Computer Vision and Pattern Recognition*, pages 4368–4377, 2021. 2
- [29] Feiwei Qin, Zhengwei Shen, Ruiquan Ge, Kai Zhang, Fei Lin, Yeru Wang, Juan M Gorriz, Ahmed Elazab, and Changmiao Wang. Infraffin: A feature fusion network leveraging dual-path convolution and self-attention for infrared image super-resolution. *Knowledge-Based Systems*, 310:112960, 2025. 5, 6
- [30] Chao Qu, Xiaoyu Chen, Qihan Xu, and Jing Han. Frequency-aware degradation modeling for real-world thermal image super-resolution. *Entropy*, 26(3):209, 2024. 2
- [31] Yunpeng Qu, Kun Yuan, Jinhua Hao, Kai Zhao, Qizhi Xie, Ming Sun, and Chao Zhou. Visual autoregressive modeling for image super-resolution. *arXiv preprint arXiv:2501.18993*, 2025. 2, 3, 4, 5, 6, 7
- [32] Ali Razavi, Aaron Van den Oord, and Oriol Vinyals. Generating diverse high-fidelity images with vq-vae-2. *Proceedings of the Advances in Neural Information Processing Systems*, 32, 2019. 3
- [33] GH Rieke, M Blaylock, Leen Decin, C Engelbracht, P Ogle, E Avrett, J Carpenter, RM Cutri, L Armus, K Gordon, et al. Absolute physical calibration in the infrared. *The Astronomical Journal*, 135(6):2245, 2008. 2
- [34] Enrique Sanchez and et al. Hadji. Multi-scale image super resolution with a single auto-regressive model. *arXiv preprint arXiv:2506.04990*, 2025. 2
- [35] Yu Shi, Yu Liu, Juan Cheng, Z Jane Wang, and Xun Chen. Vdmufusion: A versatile diffusion model-based unsupervised framework for image fusion. *IEEE Transactions on Image Processing*, 34:441–454, 2024. 2
- [36] Oriane Siméoni, Huy V. Vo, Maximilian Seitzer, Federico Baldassarre, Maxime Oquab, Cijo Jose, Vasil Khalidov, Marc Szafraniec, Seungeun Yi, Michaël Ramamonjisoa, Francisco Massa, Daniel Haziza, Luca Wehrstedt, Jianyuan Wang, Timothée Darcet, Théo Moutakanni, Leonel Sentana, Claire Roberts, Andrea Vedaldi, Jamie Tolan, John Brandt, Camille Couprie, Julien Mairal, Hervé Jégou, Patrick Labatut, and Piotr Bojanowski. DINOv3, 2025. 3
- [37] Yang Song, Jascha Sohl-Dickstein, Diederik P Kingma, Abhishek Kumar, Stefano Ermon, and Ben Poole. Score-based generative modeling through stochastic differential equations. *arXiv preprint arXiv:2011.13456*, 2020. 2
- [38] Keyu Tian, Yi Jiang, Zehuan Yuan, Bingyue Peng, and Liwei Wang. Visual autoregressive modeling: Scalable image generation via next-scale prediction. *Proceedings of the Advances in Neural Information Processing Systems*, 37:84839–84865, 2024. 3, 4
- [39] Aaron Van Den Oord, Oriol Vinyals, et al. Neural discrete representation learning. *Proceedings of the Advances in Neural Information Processing Systems*, 30, 2017. 3, 4
- [40] Jianyi Wang, Zongsheng Yue, Shangchen Zhou, Kelvin CK Chan, and Chen Change Loy. Exploiting diffusion prior for real-world image super-resolution. *International Journal of Computer Vision*, 132(12):5929–5949, 2024. 2, 5
- [41] Xintao Wang, Liangbin Xie, Chao Dong, and Ying Shan. Real-esrgan: Training real-world blind super-resolution with pure synthetic data. In *Proceedings of the IEEE/CVF International Conference on Computer Vision*, pages 1905–1914, 2021. 2
- [42] Yufei Wang, Wenhan Yang, Xinyuan Chen, Yaohui Wang, Lanqing Guo, Lap-Pui Chau, Ziwei Liu, Yu Qiao, Alex C Kot, and Bihan Wen. Sinsr: diffusion-based image super-resolution in a single step. In *Proceedings of the IEEE/CVF Conference on Computer Vision and Pattern Recognition*, pages 25796–25805, 2024. 2, 5, 6
- [43] Zhou Wang, Alan C Bovik, Hamid R Sheikh, and Eero P Simoncelli. Image quality assessment: from error visibility to structural similarity. *IEEE Transactions on Image Processing*, 13(4):600–612, 2004. 5
- [44] Zhihao Wang, Jian Chen, and Steven CH Hoi. Deep learning for image super-resolution: A survey. *IEEE Transactions on Pattern Analysis and Machine Intelligence*, 43(10):3365–3387, 2020. 2
- [45] Zirui Wang, Jiayi Zhang, Tianwei Guan, Yuhan Zhou, Xingyuan Li, Minjing Dong, and Jinyuan Liu. Efficient rectified flow for image fusion. *arXiv preprint arXiv:2509.16549*, 2025. 2
- [46] Rongyuan Wu, Tao Yang, Lingchen Sun, Zhengqiang Zhang, Shuai Li, and Lei Zhang. Seesr: Towards semantics-aware real-world image super-resolution. In *Proceedings of the IEEE/CVF Conference on Computer Vision and Pattern Recognition*, pages 25456–25467, 2024. 2
- [47] Yu-Syuan Xu, Shou-Yao Roy Tseng, Yu Tseng, Hsien-Kai Kuo, and Yi-Min Tsai. Unified dynamic convolutional network for super-resolution with variational degradations. In *Proceedings of the Computer Vision and Pattern Recognition Conference*, pages 12496–12505, 2020. 2

- [48] Sidi Yang, Tianhe Wu, Shuwei Shi, Shanshan Lao, Yuan Gong, Mingdeng Cao, Jiahao Wang, and Yujiu Yang. Maniqa: Multi-dimension attention network for no-reference image quality assessment. In *Proceedings of the IEEE/CVF Conference on Computer Vision and Pattern Recognition*, pages 1191–1200, 2022. 5
- [49] Tao Yang, Rongyuan Wu, Peiran Ren, Xuansong Xie, and Lei Zhang. Pixel-aware stable diffusion for realistic image super-resolution and personalized stylization. In *Proceedings of the European Conference on Computer Vision*, pages 74–91. Springer, 2024. 2
- [50] Zengyi Yang, Yafei Zhang, Huafeng Li, and Yu Liu. Instruction-driven fusion of infrared–visible images: Tailoring for diverse downstream tasks. *Information Fusion*, 121: 103148, 2025. 2
- [51] Zongsheng Yue, Jianyi Wang, and Chen Change Loy. Resshift: Efficient diffusion model for image super-resolution by residual shifting. *Proceedings of the Advances in Neural Information Processing Systems*, 36:13294–13307, 2023. 8
- [52] Kai Zhang, Wangmeng Zuo, and Lei Zhang. Learning a single convolutional super-resolution network for multiple degradations. In *Proceedings of the Computer Vision and Pattern Recognition Conference*, pages 3262–3271, 2018. 2
- [53] Kai Zhang, Jingyun Liang, Luc Van Gool, and Radu Timofte. Designing a practical degradation model for deep blind image super-resolution. In *Proceedings of the IEEE/CVF International Conference on Computer Vision*, pages 4791–4800, 2021. 2
- [54] Richard Zhang, Phillip Isola, Alexei A Efros, Eli Shechtman, and Oliver Wang. The unreasonable effectiveness of deep features as a perceptual metric. In *Proceedings of the IEEE/CVF Conference on Computer Vision and Pattern Recognition*, pages 586–595, 2018. 5
- [55] Yulun Zhang, Kunpeng Li, Kai Li, Lichen Wang, Bineng Zhong, and Yun Fu. Image super-resolution using very deep residual channel attention networks. In *Proceedings of the European Conference on Computer Vision*, pages 286–301, 2018. 2
- [56] Liang Zhou, Zhidong Jiao, Yuchun He, Xingyue Zhu, Weipeng Sun, Xingyuan Li, and Yang Zou. Adversarially robust fourier-aware multimodal medical image fusion for lsci. *Neurocomputing*, page 131889, 2025. 2
- [57] Yang Zou, Zhixin Chen, Zhipeng Zhang, Xingyuan Li, Long Ma, Jinyuan Liu, Peng Wang, and Yanning Zhang. Contourlet refinement gate framework for thermal spectrum distribution regularized infrared image super-resolution. *International Journal of Computer Vision*, 134(1):23, 2026. 2
- [58] Yang Zou, Xingyue Zhu, Kaiqi Han, Jun Ma, Xingyuan Li, Zhiying Jiang, and Jinyuan Liu. Hatir: Heat-aware diffusion for turbulent infrared video super-resolution. *arXiv preprint arXiv:2601.04682*, 2026. 2